AIAA 2003-3592

Streamwise-Vortex Instability and Transition on the Hyper-2000 Scramjet Forebody

Shin Matsumura and Steven P. Schneider
School of Aeronautics and Astronautics
Purdue University
West Lafayette, IN 47907-1282 USA

Scott A. Berry
NASA Langley Research Center
Hampton, VA 23681

33rd AIAA Fluid Dynamics Conference and Exhibit
23–26 June 2003
Orlando, FL

Streamwise-Vortex Instability and Transition
On the Hyper-2000 Scramjet Forebody

Shin Matsumura[*] and Steven P. Schneider[+]
School of Aeronautics and Astronautics
Purdue University
West Lafayette, IN 47906 USA
and
Scott A. Berry[∞]
NASA Langley Research Center
Hampton, VA 23681, USA

ABSTRACT

Despite the closely coupled multidisciplinary design of hypersonic airbreathing vehicles, the boundary layer transition mechanisms that are important on the forebody ahead of the scramjet inlet are not well understood. The present paper investigates transition induced by the growth of streamwise vortices on a scramjet forebody geometry similar to the Hyper-X. Characteristics of the separation zone near the first compression corner are visualized with oil-flow experiments. These experiments also reveal the presence of regularly spaced streamwise vortices on the compression ramp even in the absence of controlled disturbance generators. The growth and decay of these vortices are inferred from the heat-transfer rates measured using temperature-sensitive-paints. The streamwise vortices are enhanced in a controlled and repeatable manner by wrapping tapes around the leading edge. The vortices grow significantly on the second compression ramp and then decay, suggesting transition onset. The disturbance growth seems to show a systematic trend with unit Reynolds number, although this trend was not consistently seen for all cases. For some of the cases, the disturbances showed the largest growth when the roughness spacing was close to the vortex spacing seen in the oil-flow images.

INTRODUCTION

Laminar-turbulent transition in hypersonic boundary layers is important for prediction and control of heat transfer, skin friction, and other boundary layer properties. However, for most flight vehicle applications the mechanisms leading to transition are still poorly understood. Applications hindered by this lack of understanding include reusable launch vehicles [1], high-speed interceptor missiles [2], hypersonic cruise vehicles [3], and ballistic reentry vehicles [4].

Many transition experiments have been carried out in conventional ground-testing facilities over the past 50 years. However, these experiments are contaminated by the high levels of noise that radiate from the turbulent boundary layers normally present on the wind tunnel walls [5]. These noise levels, typically 0.5-1 % of the mean, are an order of magnitude larger than those observed in flight [6, 7]. These high noise levels can cause transition to occur an order of magnitude earlier than in flight [5, 7]. In addition, the mechanisms of transition operational in small-disturbance environments can be changed or bypassed altogether in high-noise environments; these changes in the mechanisms can change the parametric trends in transition [6].

Only in the last two decades have low-noise supersonic wind tunnels been developed [5, 8]. This

---

[*] Research Assistant, Student Member, AIAA.
[+] Associate Professor, Associate Fellow, AIAA.
[∞] Visiting Researcher, NASA Langley Research Center

American Institute of Aeronautics and Astronautics

development has been difficult, since the test-section-wall boundary layers must be kept laminar in order to avoid high levels of eddy-Mach-wave acoustic radiation from the normally present turbulent boundary layers. A Mach 3.5 tunnel was the first to be successfully developed at NASA Langley [9]. Langley then developed a Mach 6 quiet nozzle [10]. Unfortunately, this pilot facility was removed from service in anticipation of a newer, higher Mach number facility (which was unsuccessful) and is presently being considered for re-commision. No hypersonic quiet tunnels are presently operational anywhere in the world. In addition, few measurements of the mechanisms leading to transition have been made in any hypersonic or supersonic facilities.

The general prediction of transition based on simulations of the transition mechanisms is a very complex and difficult problem. There are several known receptivity mechanisms, several different known forms of instability waves, many different parameters that affect the mean flow and therefore modify the stability properties, and many known nonlinear breakdown mechanisms. The parameter space is large. To focus research into potentially useful problems, generic unit problems should be carefully identified. The scramjet-vehicle forebody is one of the generic geometries that appear to be representative of vehicles of current interest.

MODEL GEOMETRY SELECTION

To improve our ability to simulate the mechanisms of transition, we need to select a geometry to use for detailed measurements and computations of the flow physics; in other words, for use in `building-block experiments' [11]. For low speed work on the cross-flow instability, Saric selected a specific 3D wing at a specific condition in order to study cross-flow waves in isolation, without interaction with TS waves [12]. Measurements of this type are clearly needed in high-speed flow, and will be very important to the process of building up validated codes and a clear understanding of the transition processes.

In the low-speed case, however, the cross-flow instability was already known to be a major mechanism in swept-wing transition. What mechanisms are dominant for representative vehicles at hypersonic speeds? Which mechanisms should be selected for such detailed studies of single wave types? *The dominant transition mechanisms on representative flight vehicles are not known.* It therefore seems critical to establish a link between designers who work with representative vehicle shapes, and researchers at

work on the understanding and simulation of various transition mechanisms.

It was thought best to obtain the geometry from the designers themselves. A number of designers and applied researchers were contacted as part of the geometry-search effort. The final generic geometry was obtained from the Hyper-X Program Office at NASA Langley, through Charles McClinton. The geometry is called the `Hyper2000', which is `*representative of the Hyper-X class of vehicles.'* It is unclassified and releasable to the public, an important feature of a geometry that is to be studied in an academic institution with basic research funding.

PROPERTIES OF THE FLOWFIELD ON A GENERIC FOREBODY

A detailed review of the literature for transition on geometries similar to the scramjet forebody is presented in Ref. [13]. This review is summarized here. Only one quiet-flow test of a scramjet forebody is reported in the open literature, and the information presented there is very limited [14]. The model was a National Aerospace Plane (NASP)-like geometry and was tested in the Langley Mach 3.5 quiet tunnel. It had a 0.012-inch radius nose on a 3.6-degree wedge forebody, followed by unspecified compression ramps. Measurements in the region past the first corner showed length transition Reynolds numbers of about 6 million for quiet conditions, and about half that under noisy conditions. Forward of the first corner, on the centerline, transition did not occur under quiet-flow conditions. Transition did occur forward of the corner off the centerline.

Although few data have so far been obtained for the flowfield on the Hyper2000, Scott Berry from NASA Langley has published measurements on the Hyper-X, which has a very similar geometry [15-17]. Taken as a whole, the data suggest the following picture. The flow leading to the first corner is mostly in the streamwise direction, with little spanwise cross-flow. The first compression angle is large enough to separate the laminar boundary layer and forms a separation bubble. The bubble affects the flow near the surface, as does the change in spanwise pressure gradient presumably associated with the increased wedge angle downstream of the corner. The amount of cross-flow increases past the first corner, with the amount of cross-flow that occurs being dependent on the properties of the boundary layer entering the first ramp, downstream of the first corner. The second corner does not seem to cause any dramatic changes. Since the Mach-6 oil-flow seems generally similar to the Mach-10 data, these appear to be generic effects.

2

These data suggest that a possible instability mechanism might involve streamwise vorticity, initially generated at or near the leading edge (or from trips) that is enhanced by or interacts with an instability associated with the shear layer above the initial separation zone, and possibly coupling with a cross-flow and/or Görtler instability. This seems particularly likely, since for reattaching shear layers above separation bubbles that can occur in compression corners, vorticity from the leading edge is known to be a triggering mechanism [13]. Streamwise vortices are commonly observed in heat-transfer rate measurements at reattachment; these are presumably generated by an unknown instability in the shear-layer [18, 19]. Detailed study of these streamwise vortices using IR imaging showed that their location can be unambiguously connected to small flows in the leading edge [20]. The Mack modes are also relevant for this geometry, but the role of streamwise vorticity in the instability and transition process was selected for detailed and isolated experimental study here.

THE BOEING/AFOSR MACH-6 QUIET TUNNEL

Quiet facilities require low levels of noise in the inviscid flow entering the nozzle through the throat, and laminar boundary layers on the nozzle walls. These features make the noise level in quiet facilities an order of magnitude lower than in conventional facilities. To reach these low noise levels, conventional blow-down facilities must be extensively modified. Requirements include a 1 micron particle filter, a highly polished nozzle with bleed slots for the contraction-wall boundary layer, and a large settling chamber with screens and sintered-mesh plates for noise reduction [5]. To reach these low noise levels in an affordable way, the Purdue facility has been designed as a Ludwieg tube [21].

A Ludwieg tube is a long pipe with a converging-diverging nozzle on the end, from which flow exits into the test section (Figure 1). A diaphragm is placed downstream of the test section. When the diaphragm bursts, an expansion wave travels upstream through the test section into the driver tube. Since the flow remains quiet after the wave reflects from the contraction, sufficient vacuum can extend the useful runtime to many cycles of expansion-wave reflection, during which the pressure drops quasi-statically. More information about this facility can be found in Refs. [13 and 22].

Currently quiet-flow is attainable only at very low unit Reynolds numbers, on the order of 200,000 /ft, which is below the Reynolds numbers of interest here.

Therefore, the present data is obtained under "noisy" conditions similar to what would be obtained in a conventional hypersonic facility.

THE HYPER-2000 MODEL

The Hyper-2000 model consists of three compression surfaces and the chines. It is truncated at the combustor cowl. The compression surfaces have angles of 2.5, 8, and 11 deg. to the freestream, with the model at zero angle of attack; these angles are the same as the Hyper-X geometry. A simplified schematic of the compression ramp portion is shown in Figure 2, which is adapted from Figure 1 in Ref. [13]. The windward surface of the Hyper-2000 model is shown in Figure 3. The model has been spray-painted white in this picture. The model was machined at the Aerospace Sciences machine shop at Purdue University from standard 6061-T6 aluminum to reduce machining costs. A 3-axis CNC mill was used, as a 5-axis machine was not available. The model is 11.79 inches long, and has a span of 5.619 inches at the trailing edge. The compression surfaces are flat over a span of 2.85 inches. The model is approximately a $1/5^{th}$ scale of the full-scale vehicle.

The leading edge has a square cross-section, and not a smooth radius. This leading edge geometry is the result of the tool-bit path used during the manufacture, where the windward and leeward surfaces of the model were machined first, and then the perimeter of the model was milled out from the aluminum block. The thickness of the leading edge at several spanwise stations was measured by pressing the model into a lead sheet, a technique used earlier in Ref. [23]. The resulting profiles left in the lead sheet were examined under a 40X optical comparator. Measurements of the leading edge thickness along the span are shown in Figure 4. The thickness varies from about 0.008 to about 0.012 inches. The measurements are believed to be accurate to about 0.0005 inches. These measurements result in a mean leading edge thickness of 0.011 inches with an RMS value of 0.001 inches. There is a definite spanwise taper in the leading edge thickness. The left side of the model as seen from the front is slightly thinner.

The compression angles on the Hyper-2000 are identical to those of the Hyper-X model. However, the relative lengths of the first and second compression ramps are slightly different. This discrepancy was also verified in the original CAD file received from LaRC, ruling out the possibility of a faulty manufacture of the model. The first ramp extends 7.25 inches. from the leading edge, followed by the second ramp, which extends 2.40 inches. For the Hyper-X model, the first

3

ramp extends 12.433 inches from the virtual nose, and the second ramp is 5.334 inches [16]. When the lengths of these two models are non-dimensionalized by the total length from the nose to the end of the second ramp, the lengths of the first compression ramps are 0.75 and 0.70 for the Hyper-2000 and the Hyper-X respectively. This shows that the first compression ramp is relatively longer on the Hyper-2000 model. The reason for this mismatch is not known, but it may be one of the changes made to the Hyper-X geometry so that it would be publicly releasable.

EXPERIMENTAL METHODS AND SETUP

Two sets of experiments were performed as part of this research effort. First, oil-flow visualization was performed to get an overall understanding of the flowfield. These were performed to characterize the separation zone and whether streamwise vortices would be present on a smooth model. The second set of experiments was performed using temperature-sensitive-paints (TSP) to measure the surface temperature distribution. The general TSP technique is documented in several excellent papers such as Refs. [24-26], and the details of the measurement technique and data reduction methods specific to this facility are discussed in Ref. [27-29], and only an overview will be given here. All experiments were performed with the model at two degrees angle of attack, as in the Langley tests on the Hyper-X [15].

Two slightly different approaches for conducting oil-flow tests were attempted. The first and most common technique utilizes small dots of oil to trace out the surface streamlines. The oil is typically pigmented to maximize contrast with the background model surface, and here a pink fluorescent pigmentation was used (Dayglo Color Corp.). Since this facility has a limited run time (typically 7-8 seconds), this technique did not adequately reveal the separation line or any vortices with 200 cs viscosity oil. Lower viscosity oils could be used, but there was a concern that it could damage the Plexiglas window.

With the second painted-oil approach, the pigmented oil is simply spread evenly over the model surface with a large paintbrush. Due to a much larger volume of oil on the surface, the accumulation lines representative of flow separation and the attenuation lines representative of vortex scrubbing develop much faster. The major drawback of this second approach is that the surface streamlines are harder to detect within the overall oil movement. A video camera was used throughout each run to record the development of flow features, and a digital camera was also used to take higher resolution images just prior to tunnel unstart.

In the TSP experiments, the presence of streamwise vortices is inferred from the streaks of increased heat-transfer rate seen in the acquired images. The TSP coated model is illuminated with an excitation light source (ISSI LM4 464 nm Blue LED), and the luminescence from the TSP is recorded using a 12-bit CCD camera (Photometrics Sensys 0401E). This setup is shown in Figure 5. A reference image (wind-off) is taken at vacuum conditions while the model is believed to be at an isothermal temperature, which is measured with a thermocouple mounted on the base of the model. This image is then ratioed with the image taken during the tunnel run (wind-on). This process is necessary in this intensity-based method to eliminate most of the effects from the non-uniform lighting and paint-layer. A calibration is then applied to this intensity ratio to obtain the temperature distribution. The calibration for Dichlorotris(1,10-phenanthroline) ruthenium(II) hydrate (or Ru(phen) for short), the TSP luminophore in use, is shown in Figure 6.

The TSP coating is spray-painted over an insulating layer. This reduces the heat transfer between the TSP layer and the model, which enhances the surface temperature gradient. Both layers consist of polyurethane-based auto-paint (DuPont Chroma Clear). Titanium dioxide powder (DuPont Ti-Pure R-900) is mixed in to the insulating layer to give it a bright white reflective finish. The insulator layer is polished prior to applying the TSP coat. Registration marks for the image-processing are then applied to precise coordinates using a milling machine.

Controlled streamwise vorticity is induced by wrapping strips of dry transfer-lettering tapes around the leading edge. This repeatable technique for introducing disturbances was adapted from Ref. [30], and allows controlling the downstream disturbances by varying the height and spacing of the tapes. The concept is adapted from the low-speed cross-flow work of Saric et al. [31], where it has been very productive. The spacings tried for the present research were approximately 0.21, 0.18, 0.16, 0.14, and 0.125 inches, which correspond to applying 13, 15, 17, 19, and 21 strips equally spaced respectively, with the two outer strips placed 1.25 inches from the centerline. Three thicknesses of 1.25, 1.75, and 2.25 mils were used, by stacking 5, 7, and 9 layers of transfer-lettering strips. For each combination of the spacing and thickness, tunnel runs were performed at initial total pressures of 79.5, 92.0, 104.5, 117.0, and 129.5 psia. These total pressures results in unit Reynolds numbers of approximately 1.67, 1.93, 2.20, 2.46, and 2.72 million/ft, all with an initial total temperature of 779 deg. R. The oil-flow experiments were all performed

4

with no roughness applied, and at the same total conditions.

DATA REDUCTION METHOD

Image misalignments and distortion effects from the curved window are corrected with an image registration technique. The images are directly mapped onto a two-dimensional grid, which is constructed by isometrically projecting the coordinates of the registration marks to a plane perpendicular to the back surface of the model. This technique essentially eliminates the z-coordinate of the registration marks, or the depth of the marks in and out of the image. The image-processing is then done in two dimensions using the bi-quadratic equation shown in Equation 2 and 3. The unknown coefficients are solved in a least squares sense with the simulated annealing algorithm [32]. This process typically achieves a spatial accuracy of about 0.01-0.03 inches.

$$x = a_0 + a_1 x' + a_2 y' + a_3 x' y' + a_4 x'^2 + a_5 y'^2 \qquad (2)$$

$$y = b_0 + b_1 x' + b_2 y' + b_3 x' y' + b_4 x'^2 + b_5 y'^2 \qquad (3)$$

The heat-transfer rates are computed from the measured surface temperature using a one-dimensional steady-state model [33], shown in Equation 4.

$$q = \frac{k}{t}(T - T_i) \qquad (4)$$

Here q is the heat transfer rate, k is the thermal conductivity of the insulating layer, t is the thickness of the insulating layer, T is the measured surface temperature, and T_i is the model temperature measured prior to starting the tunnel. The paint thickness at several locations is measured using a coating thickness gauge (Elcometer 456). The average thickness was measured to be 3.45 mils. A thermal conductivity of 0.48 W/mK is used [34].

The computed mean heat-transfer rate distribution along the streamwise coordinate at two unit Reynolds numbers are compared to previously published CFD data [15] in Figure 7. Only the data on the first compression ramp is shown, where the boundary-layer is most likely laminar. The data presented is a spanwise average at each streamwise location. The streamwise coordinate is normalized by the full vehicle length at the model scale, and the heat-transfer rates are normalized by the Fay and Riddell stagnation point heat-transfer rate [35] on a one-foot radius sphere scaled to the model size. The figure reveals two unexpected problems with the current data. The experimental heat-transfer rates are higher than the computations by an order of magnitude, and the data for the two unit Reynolds numbers show significant variations.

Three possible sources of these discrepancies have been identified and are listed below, along with possible approaches to resolve the problem. Experiments to investigate these issues are currently being planned.

1. The insulator layer thickness can show significant variations along the surface, sometimes by a factor of 2-3. To reduce the uncertainty from this variation, the insulating layer could be replaced with an adhesive tape which would provide a constant thickness [36, 37].
2. The temperature of the model may increase significantly between tunnel startup and image acquisition. This is especially likely near the leading edge where the model is very thin. Insulating material could be applied to the leeward side to reduce the net heating to the model. A more sophisticated heat-transfer model that includes unsteady, multi-layer, and multi-dimensional effects could be used.
3. The measured temperature distribution during the run is significantly higher due to the pressure sensitivity of the TSP. The effect of pressure on the TSP luminescence is small between atmospheric and vacuum pressures, but the sensitivity from vacuum to high pressures is not known. If the response time to pressure is on the order of seconds, then it might be more accurate to take the wind-off image at high pressure.

Despite these problems, instability analysis was carried out on the available data. The fluctuating components of the spanwise heat-transfer rate distributions are normalized by the mean heat-transfer rate. This should factor out most of the error, as long as the error in the mean heat-transfer rate is present in the magnitude of the fluctuations as well.

The instabilities are quantified in terms of an RMS value of the spanwise heat-transfer rate fluctuations to get an overall sense of the magnitude of the instabilities. A more sophisticated spectral analysis is also performed using Welch's averaged periodogram method, which is a routine available in Matlab. The power spectral densities (PSD) are then integrated in the wave-number range of relevance to obtain the power content. This information is then used to quantify the growth rate of the instability waves.

OIL-FLOW VISUALIZATION RESULTS

An image taken at the highest unit Reynolds number is shown in Figure 8. This image has been processed using the image registration technique, and the color scale has been converted to grayscale in order to enhance the contrast. The separation line immediately upstream of the first compression corner is evident from the bright line, which is caused by the accumulation of the oil. The separation line seems to be symmetric about the centerline for the most part. The separation line is brighter on the lower part of the model because of the tendency of the oil to flow down the vertically-oriented model in the time it takes to prepare the tunnel after applying the oil to the model. Another flow feature which is evident is the presence of streamwise vortices on the second and third compression surfaces. The vortices first become visible about 8 inches from the leading edge, which is 0.75 inches downstream of the first compression corner. However, these vortices are not present on the first compression ramp. This might suggest that the initial disturbances, introduced by either or both the freestream noise and the leading edge, are significantly amplified by the highly unstable separation zone. This suggests that the separation bubble, and/or the streamline curvature as a result of one, has a first order impact on the instability of streamwise vortices for these geometries.

The separation line at several total pressures is digitized from the processed images, and is shown in Figure 9. A second order polynomial is fitted to each set of data. The first compression corner is also shown for reference. A slight asymmetry is present for each case, which is probably caused by the combined effects of an asymmetric leading edge, a slight yaw in the model orientation, a non-uniform oil layer, the spatial uncertainty in the image-processing of about 0.05-0.07 inches, and error in extracting the data points from the images. This makes it difficult to assess whether the separation line for the 1.93 and 2.20 million/ft cases really cross near the edges of the ramp. However, the general trend of the separation line moving upstream with increasing unit Reynolds number seems to be consistent. This is a characteristic of laminar separation bubbles, where the upstream influence of the adverse pressure gradient caused by the corner increases with Reynolds number [38, 39]. If the experiments could be performed at much higher Reynolds numbers, the separation line can be expected to start moving back downstream when the separation zone becomes transitional.

The image shown in Figure 8 does not show the reattachment point, which is another flow feature expected to influence boundary layer instability. The reattachment line is better seen in the images taken with the oil-dot technique, shown in Figures 10 and 11, for the lowest and highest unit Reynolds numbers, respectively. The separation zone is evident by the region at about 7 inches from the leading edge where the oil dots have not been washed away significantly. It is difficult to quantify the reattachment point in these images, but it is clear that the reattachment point moves downstream with increasing unit Reynolds number. Therefore, it is expected that not only will the instability of streamwise vortices increase with unit Reynolds number, but also due to the larger separation zone.

The streamwise vortices seen on the compression ramps are the "naturally" occurring disturbances on this particular model in this facility, in the sense that they appear even without any controlled disturbance generators. They probably represent the most unstable wave-number (number of cycles per unit length), which is either amplified the most, or selectively generated by the receptivity process from the combination of freestream noise, leading edge imperfections, and the flow instabilities. The spanwise distribution of the normalized fluctuating component of the RGB color values (counts) from the image in Figure 8 is extracted and shown in Figure 12, along with data taken at several unit Reynolds numbers. Here, approximately 200 pixel columns centered at 10.7 inches on the third compression ramp were averaged to reduce the background noise level. The vortices are located in the same place for all cases, showing that these disturbances are repeatable and their wave-number is not affected by the unit Reynolds number.

Approximately 12 cycles are present in this data based upon a peak to peak distance of 2.14 inches, which results in an average wave-number of 5.6 cycles/inch. The power spectral density of these fluctuations also shows a peak around 5-5.5 cycles/inch, which is shown in Figure 13. This wave-number corresponds to an average vortex spacing of 0.19 inches. It can be expected that a roughness spacing near this vortex spacing will show the earliest and/or largest growth of the streamwise vortices.

TEMPERATURE-SENSITIVE-PAINT EXPERIMENTAL RESULTS

Sample non-dimensional heat-transfer images from Ref. [27] are shown in Figures 14 and 15. These are from a preliminary set of data, and are shown as qualitative illustrations. The insulator thickness measurement was not available for these cases. Consequently, the mean heat-transfer rate on the first

compression ramp between 2.33-3.15 and 7.05-7.27 inches respectively was used to normalize the data. This process factors out the insulator thickness and thermal conductivity assuming that the values are more or less constant throughout the model surface. The total pressure and temperature for both of these runs were 118 psia and 760 deg. R. Figure 14 shows five roughness strips 4 mils thick spaced 5/8 inch apart on the leading edge and the vortices generated by them. The outer two gets swept away onto the chine by the outward directed cross-flow. Figure 15 shows a closer view of the compression corners. The breakdown of the vortices is clearly visible. Figure 16 is a sample image from the most recent set of data. The initial total pressure and temperature was 127.2 psia and 779 deg. R respectively, giving a unit Reynolds number of 2.67 million/ft. The temperature of the model and TSP layer prior to the tunnel run was 547 deg. R. The roughnesses were spaced 0.16 inches apart, each with a thickness of 2.25 mils. The increased number of vortices generated by the increased number of roughnesses is evident.

The spanwise heat-transfer rate variations in the data shown in Figure 16 are extracted and shown in Figure 17. Each set of data here has been averaged 0.45 inches streamwise (61 pixel columns) to reduce noise. For this figure, the averaging window was doubled from what is normally used for quantitative analyses, so that the fluctuations are clearly visible. These spanwise cut locations are marked with dashed lines in Figure 16. Upstream of the first corner at 6.9 inches from the leading edge, the fluctuations are very small. No preferred wavelength seems to have arisen from the noise. Then the fluctuations grow just downstream of the first corner, and the regularly spaced oscillations are clearly visible at 8.97 inches. These fluctuations correspond to the streak structures shown in Figure 16, which are apparently caused by the growth of stationary streamwise vortices. At 10.09 inches, the amplitude of the fluctuations is smaller, but the mean heat transfer rate increases. This suggests that transition has begun, although hot-wire measurements are necessary for confirmation.

The PSD's of the spanwise heat-transfer rate fluctuations at 8.97±0.225 inches are shown in Figure 18 for each of the roughness spacing cases with the largest roughness thickness and highest unit Reynolds number. As expected, the peak wave-number increases as the roughnesses are applied closer together. The peak for the 0.21 inch spacing case is not as clearly separated from the other wave-numbers due to the lower clarity of the streaks in the images. However, there seems to be a peak around 4.2 cycles/inch. Figure 19 shows the PSD's at the lowest unit Reynolds number

of 1.67 million/ft, with all other conditions the same as that of Figure 18. This figure does not show a peak at all for the largest roughness spacing of 0.21 inches. However, the peaks for the other roughness spacing are at the identical wave-numbers, showing that unit Reynolds number does not have an effect on the dominant wave-number seen at this streamwise station, as in the oil-flow experiments with no roughness.

The average spacing of the fluctuations at 8.97 inches with 2.25 mil thickness roughness as determined from the peak wave-number is shown in Figure 20. The spacing determined from visual inspection is shown as well. This value for the largest spacing has been omitted because of the difficulty in visually counting the fluctuations due to the low quality image. The error bars represent the attainable resolution in the spectral analysis, which is limited by the current CCD camera's pixel resolution. The streamwise vortices spread slightly outwards as they travel downstream, evident by the larger disturbance spacing. Figure 21 shows that this vortex spreading rate (the difference between the average roughness and disturbance spacing per streamwise distance) also increases with roughness spacing. The data shown here were computed using the values in Figure 20. This increased spreading rate with roughness spacing might imply nonlinearity in the disturbances.

Figure 22 shows the RMS statistical analysis of the spanwise heat-transfer rate fluctuations, which is an estimation of the instability growth along the streamwise coordinate. The figure is essentially a measure of the magnitude of the spanwise fluctuations. The data shown here is for the case employing 17 roughness strips (0.16 inch spacing) of 2.25 mil thicknesses. The fluctuations grow mostly on the second compression ramp immediately downstream of the first corner, and reach a peak value between 8.5-9.0 inches. The fluctuations then decay, but show a slight growth immediately past the second corner. This decay on the second ramp is one sign that suggests transition. However, it is possible that at the lower unit Reynolds numbers, transition takes place on the third compression ramp rather than on the second ramp. Also, this decay might simply be caused by the streamwise vortices lifting away from the surface near the corners due to a very small separation zone and/or adverse pressure gradient from the corner which propagates upstream. Other measurements such as hot-wire data and/or more accurate and reliable mean heating data are needed to relate the fluctuation amplitudes to the onset of transition.

This data shows that as the unit Reynolds number is increased, the streamwise coordinate corresponding to the maximum RMS fluctuations (marked by symbols

in Figure 22) moves upstream, and the maximum RMS values decrease.   These maximum RMS values are quantified for all cases in Figures 23-25. On average, the maximum fluctuations are about 6±2 % of the mean heating value.   There are no clear trends which are consistent throughout the dataset, although the results seem to become systematic as the roughness thickness is increased. This might be caused by the use of raw RMS fluctuation values. One possibility is to convert the dataset into some sort of amplitude ratio, but the initial disturbance magnitude is very difficult to quantify, because the RMS fluctuations upstream of the first corner are mostly noise.   This results in inconsistent initial disturbance magnitudes, with no physical basis.

Another possibility is that for all conditions investigated the disturbances become saturated, resulting in similar disturbance magnitudes, an effect also seen for stationary cross-flow vortices [40]. However, it is difficult to say whether the present instability data, which are inferred from measurements of the surface imprint, are accurate enough to speculate on such effects.   The fluctuations might be underpredicted here because of 2-D conduction effects due to large spatial temperature gradients caused by the streamwise vortices. Tests on the Hyper-X with gas injection for tripping the boundary-layer showed that one-dimensional heat-transfer analysis could underpredict the fluctuation magnitudes by as much as 20 % [41]. Another possibility is that noise in the spanwise heat-transfer rate distributions contaminate the RMS-values, resulting in false trends. The spectral approach might give better results, due to the filtering process in computing the power content within a specific wave-number band.

The analysis is repeated with the spectral analysis approach on the same dataset with a roughness spacing and thickness of 0.16 inches and 2.25 mils. Figure 18 showed a peak at 5.23 cycles/inch for this roughness spacing.   The streamwise variation of the power spectral density (PSD) at this wave-number is shown in Figure 26 for this roughness configuration at the highest unit Reynolds number. Also shown are the PSD's of four adjacent wave-numbers near the peak wave-number. The PSD at the peak wave-number reaches the highest value.   Also, the PSD's at 4.70 and 5.75 cycles/inch are consistently greater than the PSD's at the lowest and highest wave-numbers. The PSD in this wave-number band is integrated, and the streamwise power distribution is shown in Figure 27. The trends shown here are very similar to the trends seen in Figure 22, with the peaks on the second and third compression ramp.

The power distribution is normalized by the maximum power on the third ramp for each case, and is re-plotted in Figure 28. When the data is presented in this manner, not only does the streamwise coordinate of the maximum value move upstream with increasing unit Reynolds number, the peak on the second compression ramp grows the earliest and reaches a higher value. The variation with roughness spacing is shown in Figure 29. All cases here used a roughness thickness of 2.25 mils and unit Reynolds number of 2.72 million/ft. The case with the 0.18 inch roughness spacing shows the largest and earliest growth.   This agrees with the vortex spacing seen in the oil-flow images of 0.19 inches, which may be the most unstable wavelength. The variation of the amplitude ratio with roughness thickness is shown in Figure 30. All cases here used a roughness spacing of 0.16 inches and a unit Reynolds number of 2.72 million/ft.   The peak amplitude ratio increases with thickness, and the streamwise coordinate corresponding to it moves slightly upstream.

It is not known what this amplitude ratio physically represents, but because it seems to give reasonable and clear trends for the particular cases shown above, it was adapted as the preferred method to quantify the instability growth.   It is hoped that this is useful information that can be related to a computational analysis. Similar to the results of the RMS statistical analysis, the streamwise location where the amplitude ratio reaches a peak might be related to transition onset. These values are compared in Figure 31-33 for the complete dataset, with roughness thicknesses of 1.25, 1.75, and 2.25 mils respectively. In general, a slight decrease is seen at a roughness spacing of 0.16-0.18 inches, which is near the vortex spacing seen in the oil-flow with no roughness. If this coordinate is related to transition onset, then the values should decrease with increasing roughness thickness and unit Reynolds number.   There might also be a minimum near roughness spacing around 0.19 inches. These trends are seen for some of the cases, such as the two highest unit Reynolds numbers for the thickest roughness. However there are inconsistencies within the datasets. The data for the smallest roughness thickness seems to show the most uncertainty and scatter. This might suggest that the streamwise vortices generated by these roughness are too weak, resulting in a small heat-transfer rate increase and signal-to-noise ratio. The cases which do not show clear trends and possible correlations should be repeated after the measurement technique is refined, and transition onset information is available.

CONCLUSIONS

Oil-flow visualization and temperature-sensitive-paints measurements were used to infer the instability of streamwise vortices on a scramjet forebody model. The experiments were carried out in a conventional facility in terms of the freestream noise levels. Oil-flow visualization was used to map the separation line upstream of the first compression corner, and to measure the spacing of "naturally" occurring streamwise vortices in the absence of controlled disturbance generators. Temperature-sensitive-paint was then used to infer the presence of streamwise vortices, and the computed heat-transfer rates were used to quantify the instability.

The streamwise vortices appeared immediately after reattachment downstream of the first compression corner in the oil-flow experiments, which might suggest a Görtler-like instability mechanism. This observation is consistent with oil-flow images available from other conventional facilities such as Langley's 20-inch Mach 6. The spacing of the streamwise vortices in the oil-flow was not affected by unit Reynolds number. One would expect that changing the unit Reynolds number changes the boundary-layer thickness, which would change the spacing of the vortices as well. This lack of variation with unit Reynolds number might be an indication that the disturbances were generated from imperfections in the leading edge. On the other hand, the Hyper-X model used by Langley had a much higher quality leading edge, and showed vortices in the absence of applied roughness as well.

The quantitative measurements using temperature-sensitive-paints seem to show systematic trends, and provide information about this instability mechanism involving streamwise vortices. For all the roughness configurations and flow conditions tested here, the vortices first appeared also on the second compression ramp. The vortex spacing directly relates to the roughness spacing, and was independent of unit Reynolds number as with the oil-flow experiments. A statistical and spectral analysis showing the magnitude of the spanwise heat-transfer fluctuations seems to show a systematic trend with unit Reynolds number. As unit Reynolds number increases, the peak in the fluctuations moves upstream. However, this trend was not consistent for the entire parameter space, making it difficult to reach a definitive and generalized conclusion. Comparison with computations is needed. Whether the two sets of data agree or not, this will provide a further knowledge of this type of instability mechanism, and also help to guide future experiments which should be performed once the measurement technique is refined.

ACKNOWLEDGEMENTS

REFERENCES

[1]   Berry, S.A., Horvath, T.J., Hollis, B.R., Thompson, R.A., and Harris II, H.H. X-33 Hypersonic Boundary Layer Transition. Paper 99-3560, AIAA, June 1999.

[2]   Korejwo, H.A. and Holden, M.S. Ground Test Facilities for Aerothermal and Aero-optical Evaluation of Hypersonic Interceptors. Paper 92-1074, AIAA, February 1992.

[3]   AGARD, editor. *Sustained Hypersonic Flight*. AGARD, April 1997. CP-600, vol. 3.

[4]   Lin, T.C., Grabowsky, W.R., and Yelmgren, K.E. The Search for Optimum Configurations for Re-entry Vehicles. *J. of Spacecraft and Rockets*, 21(2):142-149, March-April 1984.

[5]   Beckwith, I.E. and Miller III, C.G. Aerothermodynamics and Transition in High-speed Wind Tunnels at NASA Langley. *Annual Review of Fluid Mechanics*, 22:419-439, 1990.

[6]   Schneider, S.P. Effects of High-Speed Tunnel Noise on Laminar-Turbulent Transition. *J. of Spacecraft and Rockets*, 38(3):323-333, May-June 2001.

[7]   Schneider, S.P. Flight Data for Boundary-Layer Transition at Hypersonic and Supersonic Speeds. *J. of Spacecraft and Rockets*, 36(1)8-20, 1999.

[8]   Wilkinson, S.P., Anders, S.G., and Chen, F.-J. Status of Langley Quiet Flow Facility Developments. Paper 94-2498, AIAA, June 1994.

[9]   Beckwith, I., Creel, T., Chen, F., and Kendall, J. Freestream Noise and Transition Measurements on a Cone in a Mach-3.5 Pilot Low-Disturbance Tunnel. Technical Paper 2180, NASA, 1983.

[10]   Blanchard, A.E., Lachowicz, J.T., and Wilkinson, S.P. NASA Langley Mach 6 Quiet-Wind Tunnel Performance. *AIAA J.*, 35(1):23-28, January 1997.

[11]   Marvin, J.G. Perspective on Computational Fluid Dynamics Validation. *AIAA J.*, 33(10):1778-1787, October 1995.

[12]   Radeztsky, R.H., Reibert, M.S., and Saric, W.S. Effect of Isolated Micron-sized Roughness on Transition in Swept-wing Flows. *AIAA J.*, 37(11):1370-1377, November 1999.

[13]   Schneider, S.P., Matsumura, S., Rufer, S., Skoch, C., and Swanson, E. Hypersonic Stability and Transition Experiments on Blunt Cones and a Generic Scramjet Forebody. Paper 2003-1130, AIAA, January 2003.

[14]   Elias, T. and Eiswirth, E. Stability Studies of Planar Transition in Supersonic Flows. Paper 90-5233, AIAA, October 1990.

[15]   Berry, S.A., Auslender, A.H., Dilley, A.D., and Calleja, J.F. Hypersonic Boundary-Layer Trip Development for Hyper-X. *Journal of Spacecraft and Rockets*, 38(6):853-864, November-December 2001.

[16]   Berry, S.A., DiFulvio, M., and Kowalkowski, K. Forced Boundary-Layer Transition on X-43 (Hyper-X) in NASA LaRC 20-Inch Mach 6 Air Tunnel. NASA TM-2000-210316, August 2000.

[17]   Berry, S.A., DiFulvio, M., and Kowalkowski, K. Forced Boundary-Layer Transition on X-43 (Hyper-X) in NASA LaRC 31-Inch Mach 10 Air Tunnel. NASA TM-2000-210315, August 2000.

[18]   Delery, J.M. and Panaras, A.G. Shock-wave/Boundary-layer Interactions in High Mach-Number Flows. In *Hypersonic Experimental and Computational Capability, Improvement and Validation*, pg. AR-319 v. I., AGARD, May 1996.

[19]   Ginoux, J. Streamwise Vortices in Reattaching High-Speed Flows: A Suggested Approach. *AIAA Journal*, 9(4):759-760, April 1971.

[20]   De Luca, L., Cardone, G., Chevalerie, D., and Fonteneau, A. Viscous Interaction Phenomena in Hypersonic Wedge Flow. *AIAA Journal*, 33(12):2293-2299, December 1995.

[21]   Schneider, S.P. and Haven, C.E. Quiet-Flow Ludwieg Tube for High-Speed Transition Research. *AIAA J.*, 33(4):688-693, April 1995.

[22]   Schneider, S.P., Rufer, S., Skoch, C., and Swanson, E. Hypersonic Transition Research in the Boeing/AFOSR Mach-6 Quiet Tunnel. Paper 2003-3450, AIAA, June 2003.

[23]   Pate, S. Dominance of Radiated Aerodynamic Noise on Boundary-Layer Transition in Supersonic-Hypersonic Wind Tunnels. AEDC-TR-77-107, March 1978.

[24]   Campbell, B.T., Liu, T., and Sullivan, J.P. Temperature Sensitive Fluorescent Paint Systems. Paper 94-2483, AIAA, June 1994.

[25]   Hamner, M. Demystifying Luminescent Paint Technology: A Guide for Non-Developers. Paper 2001-2981, AIAA, June 2001.

[26]   Liu, T., Campbell, B.T., Burns, S.P. and Sullivan, J.P. Temperature- and Pressure-Sensitive Luminescent Paints in Aerodynamics. *Applied Mechanics Review*, 50(4):227-246, April 1997.

[27]   Schneider, S.P., Matsumura, S., Rufer, S., Skoch, C., and Swanson, E.. Progress in the Operation of the Boeing/AFOSR Mach-6 Quiet Tunnel. Paper 2002-3033, AIAA, June 2002.

[28]   Matsumura, S., Berry, S.A., and Schneider, S.P. Flow Visualization Measurement Techniques for High-Speed Transition Research in the Boeing/AFOSR Mach-6 Quiet Tunnel. Paper 2003-4583 AIAA, July 2003.

[29]   Matsumura, S. Streamwise Vortex Instability and Transition on the Hyper-2000 Scramjet Forebody. MS Thesis, To Appear, School of Aeronautics and Astronautics, Purdue University, August 2003.

[30]   Ginoux, J.J. *Streamwise Vortices in laminar Flow*, pages 395-422. AGARD, 1965. AGARDograph 97.

[31]   Radeztsky, R.H., Reibert, M.S. and Saric, W.S. Effect of Isolated Micron-Sized Roughness on

Transition in Swept-Wing Flows. *AIAA J.*, 37(11):1370-1377, November 1999.

[32] Goffe, W. L., Ferrier, G. D., and Rogers, J. Global Optimization of Statistical Functions with Simulated Annealing. *Journal of Econometrics*, Vol. 60, No. 1-2, pg. 65-99, January-February 1994.

[33] Liu, T., Campbell, B.T., and Sullivan, J.P. Fluorescent Paint for Measurement of Heat Transfer in Shock-Turbulent Boundary Layer Interactions. *Experimental Thermal and Fluid Science*, 10(1):101-112, January 1995.

[34] Hubner, J.P., Carroll, B.F., and Schanze, K.S. Heat Transfer Measurements in Hypersonic Flow Using Luminescent Coating Techniques. Paper 2002-0741, AIAA, January 2002.

[35] Fay, J.A. and Riddell, F.R. Theory of Stagnation Point Heat Transfer in Dissociated Air. *Journal of Aerospace Sciences*, 25(2):73-85, 121, 1958.

[36] Crafton, J., Lachendro, N., Guille, M., Sullivan, J.P., and Jordan, J.D. Application of Temperature and Pressure Sensitive Paint to an Obliquely Impinging Jet. Paper 99-0387, AIAA, January 1999.

[37] Liu, T., Campbell, B. T., Sullivan, J. P., Lafferty, J., and Yanta, W. Heat Transfer Measurement on a Waverider at Mach 10 Using Fluorescent Paint. *AIAA Journal of Thermophysics and Heat Transfer*, 9(4):605-611, October-December 1995.

[38] Lewis, J.E., Kubota, T., and Lees, L. Experimental Investigation of Supersonic Laminar, Two-Dimensional Boundary-Layer Separation in a Compression Corner with and without Cooling. *AIAA Journal*, 6(1):7-14, January 1968.

[39] Chpoun, A. Hypersonic Flow in a Compression Corner in 2D and 3D Configurations. Paper 89-1876, AIAA, June 1989.

[40] Haynes, T.S. and Reed, H.L. Simulation of Swept-Wing Vortices Using Nonlinear Parabolized Stability Equations, J. of Fluid Mech., vol. 405, pp. 325-349, 2000.

[41] Daryabeigi, K., Berry, S.A., Horvath, T.J., and Nowak, R.J. Finite Volume Numerical Methods for Aeroheating Rate Calculations From Infrared Thermographic Data. Paper 2003-3634, AIAA, June 2003.
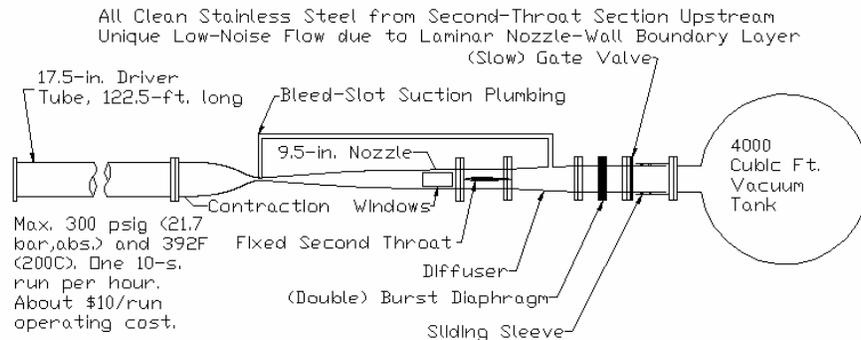
Figure 1. Schematic of the Boeing/AFOSR Mach 6 Quiet Tunnel
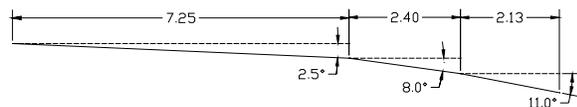
Figure 2. Sideview of the Hyper-2000 Forebody, adapted from Ref. [13]
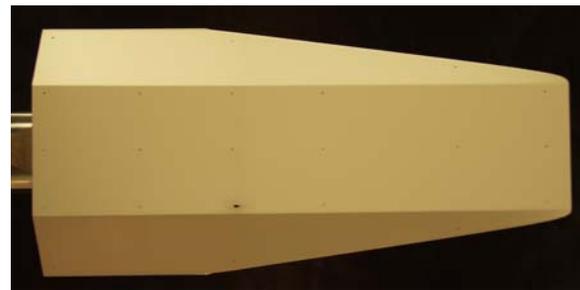
Figure 3. Picture of the Hyper-2000 Model
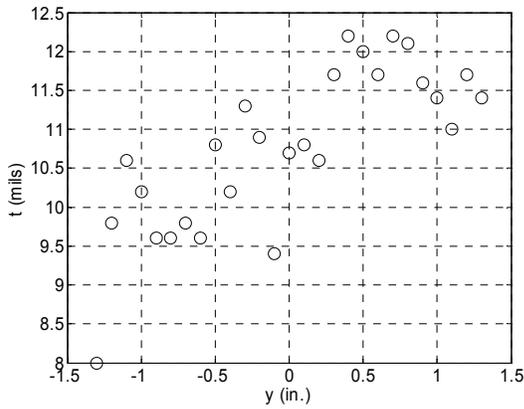
Figure 4. Leading Edge Thickness Variation

Figure 5. Experimental Setup for TSP Experiments
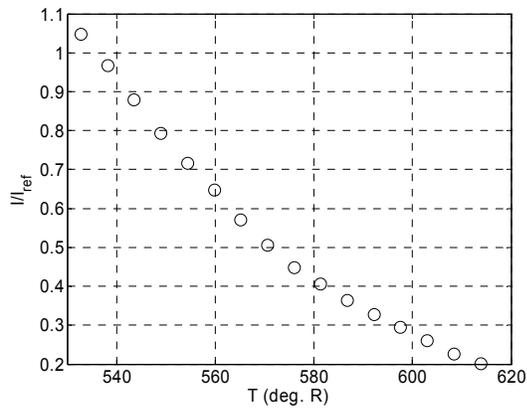
Figure 6. TSP Calibration (T_{ref} = 536 deg. R.)
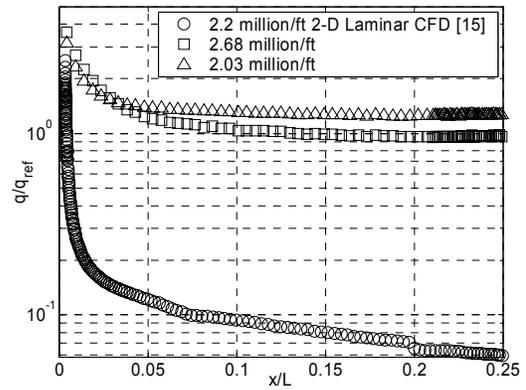
Figure 7. Comparison of Heat-Transfer Rates to CFD Data
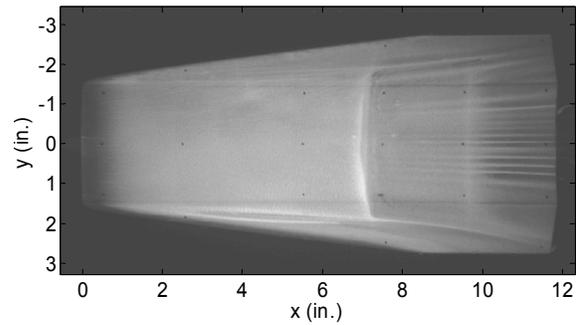
Figure 8. Oil-flow Image for Unit Reynolds number of 2.72 million/ft
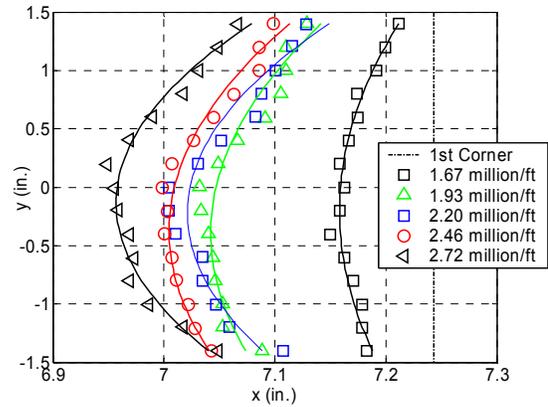
Figure 9. Unit Reynolds Number Effect on the Separation Line

12

American Institute of Aeronautics and Astronautics
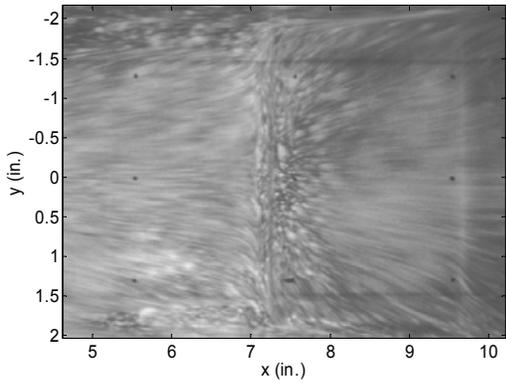
Figure 10. Oil-flow Image with the Oil-Dot Technique at the Lowest Unit Reynolds Number (1.67 million/ft)
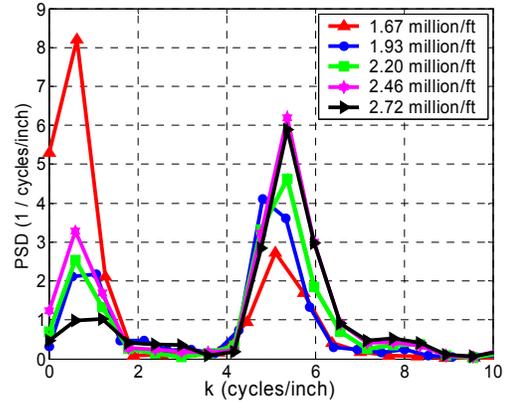
Figure 13. PSD of the Spanwise Fluctuations at 10.7 inches From the Leading Edge
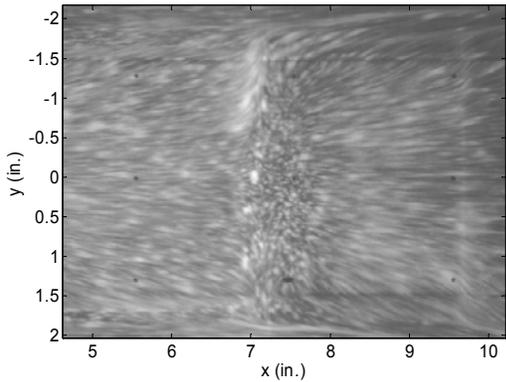
Figure 11. Oil-flow Image with the Oil-Dot Technique at the Highest Unit Reynolds Number (2.72 million/ft)
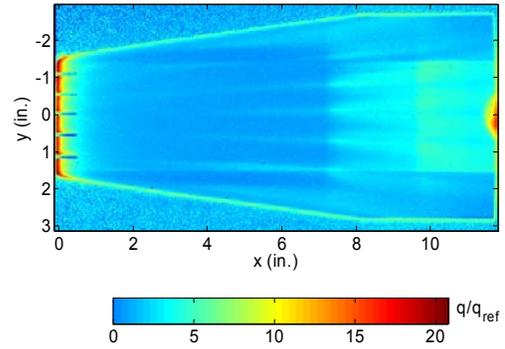
Figure 14. Normalized Heat-Transfer Rate Image with Five 4 mil Thick Roughness Spaced 5/8 inch Apart at 2.57 million/ft Unit Reynolds Number
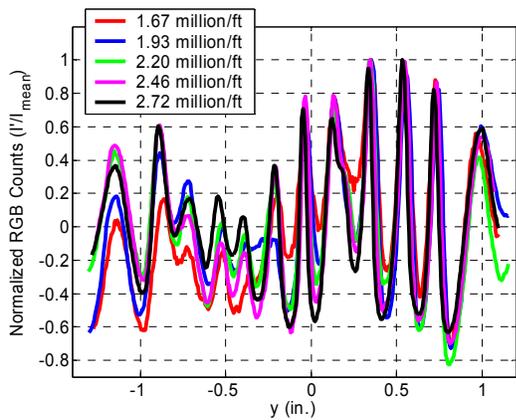
Figure 12. Spanwise Fluctuations Seen in the Oil-Flow Images, at 10.7 inches from the Leading Edge
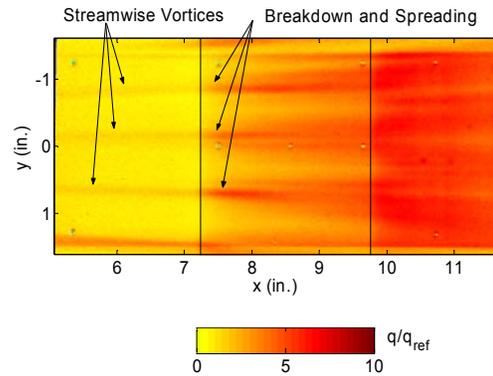
Figure 15. Normalized Heat-Transfer Rate Image with Five 4 mil Thick Roughness Spaced 5/8 inch Apart at 2.57 million/ft Unit Reynolds Number

13
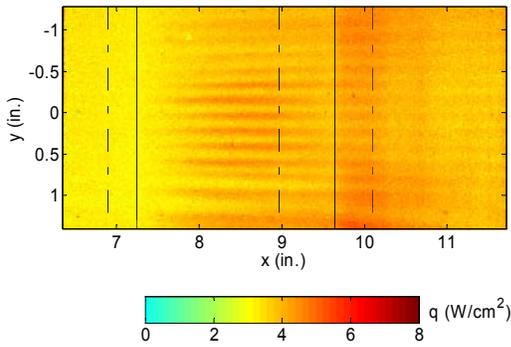
Figure 16. Heat-Transfer Rate Image with 17 Roughness (0.16 inch spacing) of 2.25 mil Thickness at Total Pressure of 127.2 psia (2.67 million/ft.)
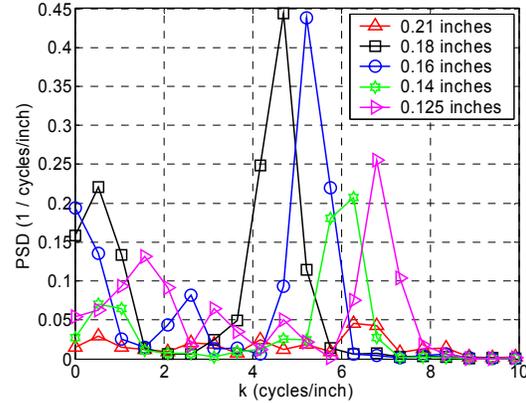
Figure 19. Power Spectral Densities of the Spanwise Heat Transfer Rate Distributions at 8.97 inches from Leading Edge with 2.25 mil Thickness Roughness at 1.67 million/ft Unit Reynolds Number
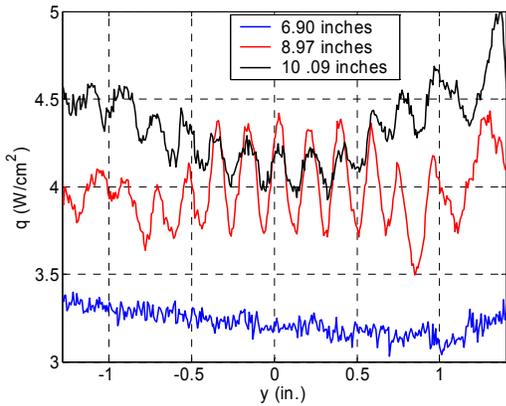
Figure 17. Spanwise Heat Transfer Rate Distributions with 2.25 mil Thick Roughness Spaced 0.16 inches at Unit Reynolds Number of 2.72 million/ft
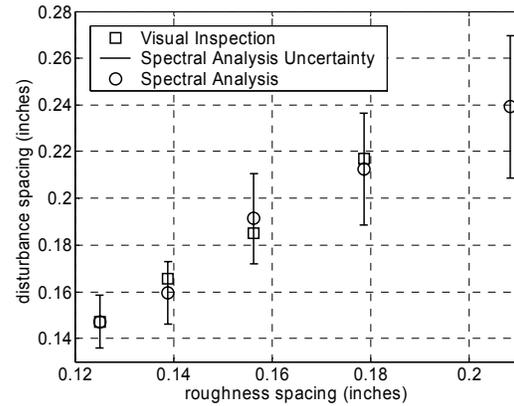
Figure 20. Average Streamwise Vortex Spacing at 8.97 inches from the Leading Edge Using 2.25 mil Thickness Roughness at 2.72 million/ft Unit Reynolds Number
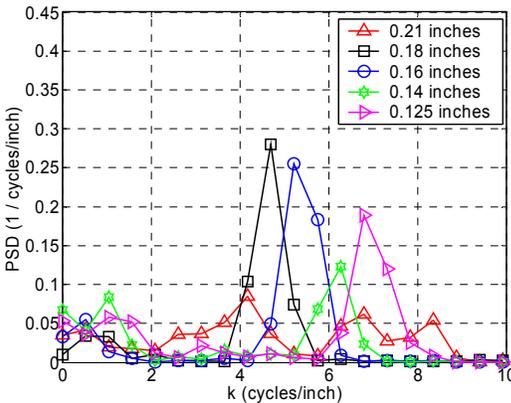
Figure 18. Power Spectral Densities of the Spanwise Heat Transfer Rate Distributions at 8.97 inches from Leading Edge with 2.25 mil Thickness Roughness at 2.72 million/ft Unit Reynolds Number
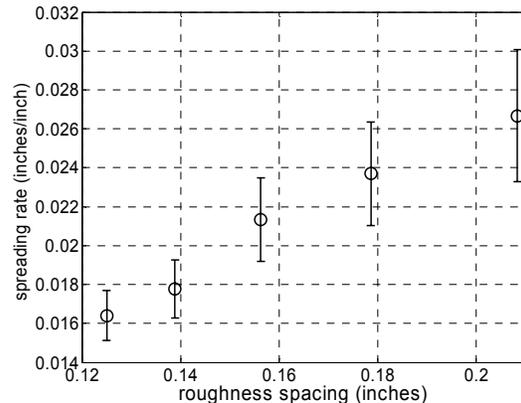
Figure 21. Average Streamwise Vortex Spreading Rate at 8.97 inches from the Leading Edge Using 2.25 mil Thickness Roughness at 2.72 million/ft Unit Reynolds Number
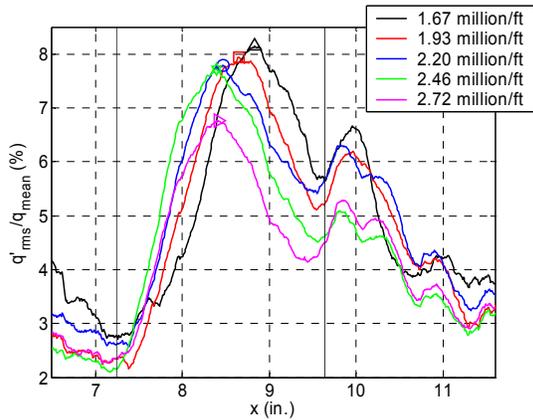
Figure 22. Streamwise Growth of the RMS-Spanwise Heat-Transfer Rate Fluctuations with 2.25 mil Thick Roughness Spaced 0.16 inches

Figure 23. Maximum Normalized RMS Fluctuations on the Second Compression Ramp with Roughness Thickness of 1.25 mils

Figure 24. Maximum Normalized RMS Fluctuations on the Second Compression Ramp with Roughness Thickness of 1.75 mils
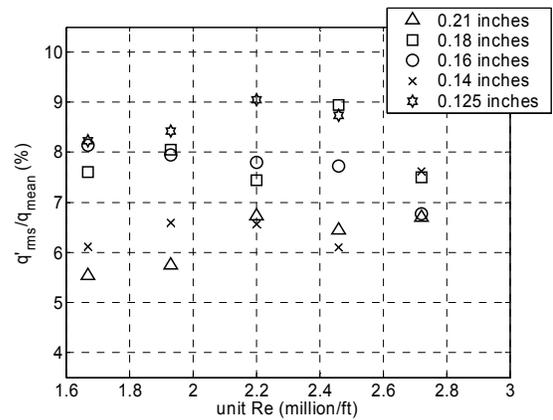

Figure 25. Maximum Normalized RMS Fluctuations on the Second Compression Ramp with Roughness Thickness of 2.25 mils
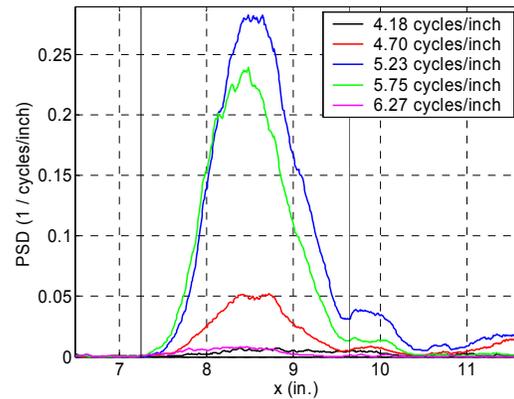
Figure 26. Streamwise Distribution of PSD's Near the Dominant Wave-number with 2.25 mil Thick Roughness Spaced 0.16 inches at Unit Reynolds Number of 2.72 million/ft
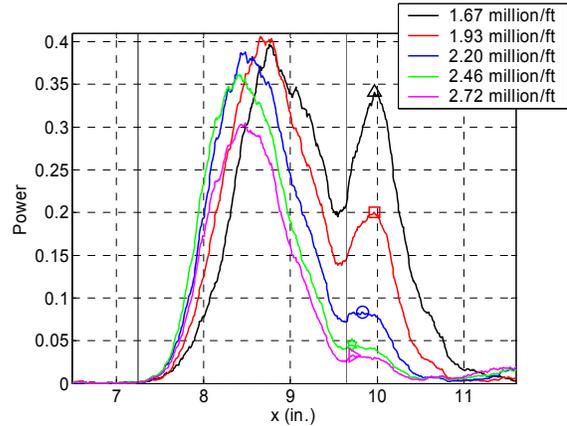
Figure 27. Streamwise Distribution of the Power with 2.25 mil Thick Roughness Spaced 0.16 inches

15
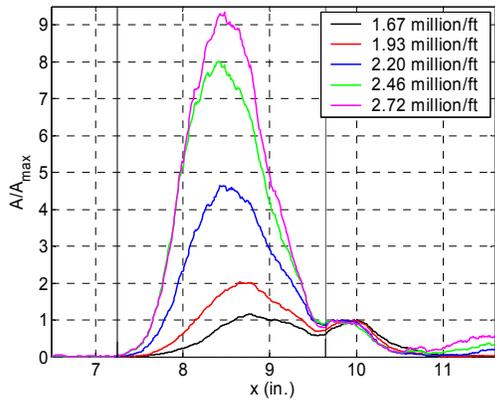
Figure 28. Streamwise Distribution of the Amplification Ratio with 2.25 mil Thick Roughness Spaced 0.16 inches at Several Unit Reynolds Numbers
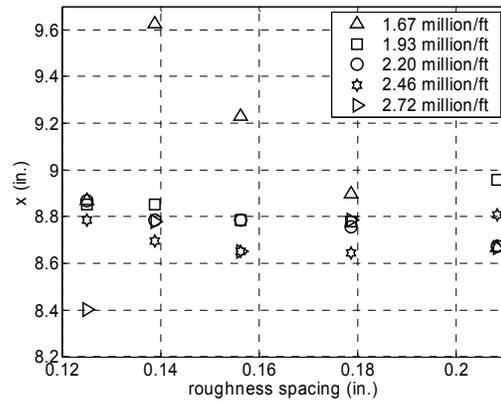

Figure 31. Streamwise Coordinates Corresponding to the Peak Amplitude Ratio with a Roughness Thickness of 1.25 mils
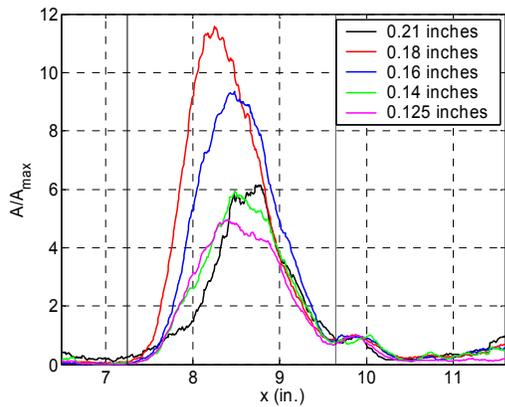

Figure 29. Streamwise Distribution of the Amplification Ratio with 2.25 mil Thick Roughness at 2.72 million/ft Unit Reynolds Number for Several Roughness Spacings
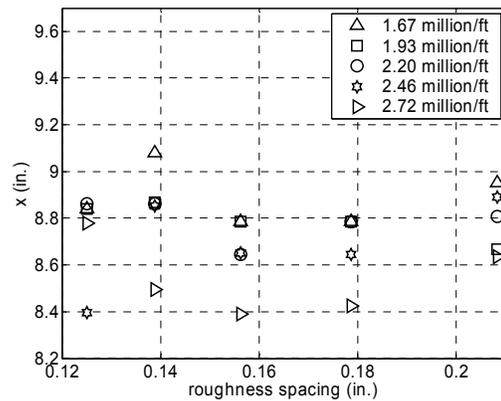

Figure 32. Streamwise Coordinates Corresponding to the Peak Amplitude Ratio with a Roughness Thickness of 1.75 mils
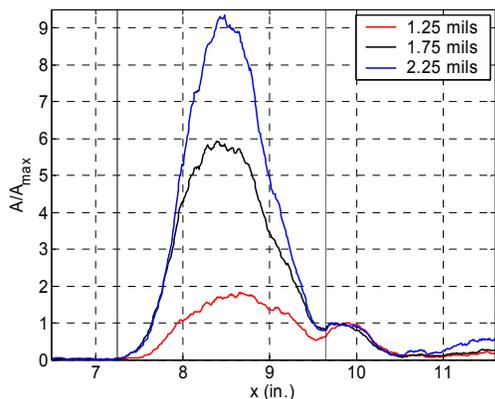

Figure 30. Streamwise Distribution of the Amplification Ratio for with Roughness Spacing of 0.16 inches and Unit Reynolds Number of 2.72 million/ft for Several Roughness Thicknesses
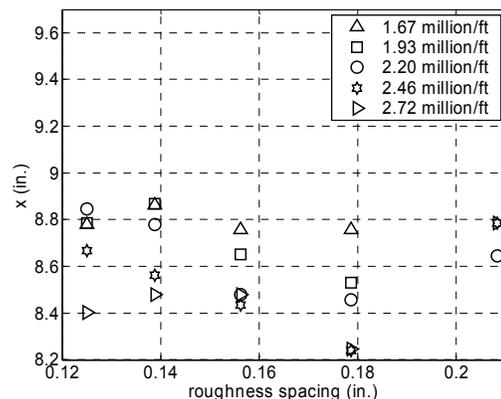

Figure 33. Streamwise Coordinates Corresponding to the Peak Amplitude Ratio with a Roughness Thickness of 2.25 mils

16